Science Advances
AAAS

advances.sciencemag.org/cgi/content/full/6/18/eaaz1192/DC1

Supplementary Materials for

Vanadium spin qubits as telecom quantum emitters in silicon carbide

Gary Wolfowicz, Christopher P. Anderson, Berk Diler, Oleg G. Poluektov, F. Joseph Heremans, David D. Awschalom*

*Corresponding author. Email: awsch@uchicago.edu

Published 1 May 2020, *Sci. Adv.* **6**, eaaz1192 (2020)
DOI: 10.1126/sciadv.aaz1192

This PDF file includes:

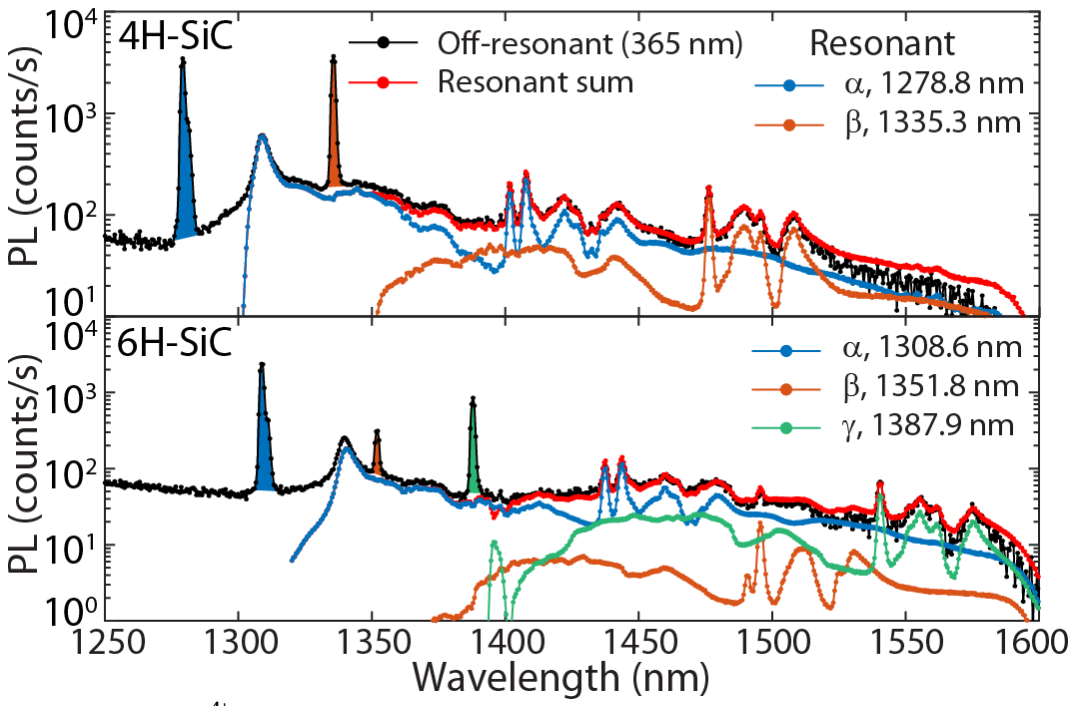

Fig. S1. Optical spectra of V^{4+} in 4H-SiC and 6H-SiC at 3.3 K using off-resonant excitation (365 nm, black) and on-resonant excitation (blue, orange, yellow). The on-resonant excitation is done for the GS1-ES1 transition with background subtraction from slightly detuned excitation. The curve in red provides the sum of the resonant contributions with weights fitted to match the off-resonant excitation. The colored area under the various zero-phonon lines and the resonant spectra are integrated to calculate the Debye-Waller factor. The error in this factor from the missing spectra at longer wavelength is estimated to be less than 10 % by Gaussian extrapolation (*16*).

Section S1. Isotope model

We model the lineshape of the optical transitions by the presence of minority isotopes within the two nearest neighbor shells of the vanadium impurity as illustrated in Fig. S2. Starting from a pure lattice of ^{28}Si and ^{12}C, any local change to ^{29}Si, ^{30}Si or ^{13}C leads to a mass and observed linewidth shift. We assume the following:

1. The samples have natural abundance of silicon and carbon atoms.
2. Only the first carbon and silicon shells have a significant influence on the electronic wavefunction.
3. Each Si and C sites are equivalent. This simplifies the model, but it is likely that the c-axis bonds may be different from the basal bonds.
4. One ^{30}Si corresponds to two unit of mass shifts, or equivalently two ^{29}Si.
5. The mass shifts add linearly with each additional local change in isotope.

This leads to the following probability of obtaining a given configuration (and therefore PL intensity):

$$P\left(N_{^{29}Si}, N_{^{30}Si}, N_{^{13}C}\right) = \frac{N_{Si}!\left(1-f_{^{29}Si}-f_{^{30}Si}\right)^{N_{Si}-N_{^{29}Si}-N_{^{30}Si}} f_{^{29}Si}^{N_{^{29}Si}} f_{^{30}Si}^{N_{^{30}Si}}}{\left(N_{Si}-N_{^{29}Si}-N_{^{30}Si}\right)!N_{^{29}Si}!N_{^{30}Si}!} \times \frac{N_C!\left(1-f_{^{13}C}\right)^{N_C-N_{^{13}C}} f_{^{13}C}^{N_{^{13}C}}}{\left(N_C-N_{^{13}C}\right)!N_{^{13}C}!}$$

Where $N_{^{29}Si} = 0...N_{Si}$, $N_{^{30}Si} = 0...N_{Si}$ and $N_{^{13}C} = 0...N_C$ are the number of nearest neighbors ^{29}Si, ^{30}Si and ^{13}C respectively, with $N_{Si} = 12$ and $N_C = 4$ the number of silicon and carbon inequivalent sites. $f_{^{29}Si} = 0.04685$, $f_{^{30}Si} = 0.03092$ and $f_{^{13}C} = 0.0107$ are the natural abundance fraction of ^{29}Si, ^{30}Si and ^{13}C respectively.

This model provides the relative intensity between each configuration. In order to fit the spectral lineshape in Fig. 1 of the manuscript, we also use a fixed pseudo-Voigt lineshape (mostly Gaussian) for the sub-peak from a single configuration.

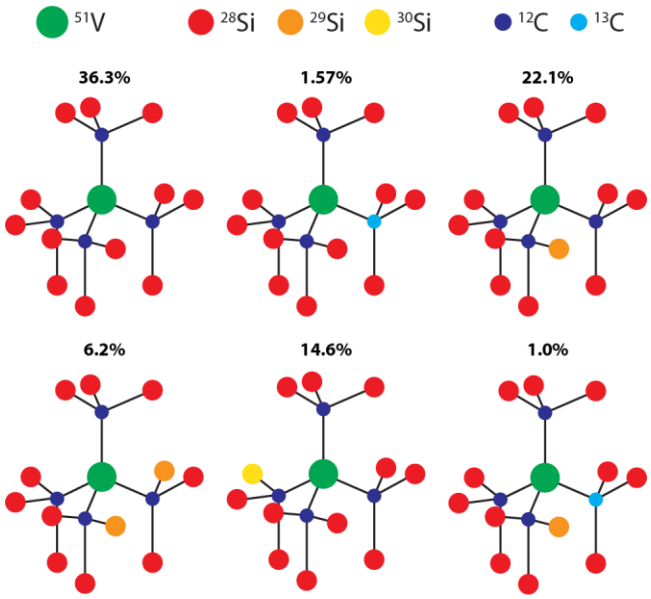

Fig. S2. Isotope model. Sample of possible isotopic distributions for the nearest-neighbor silicon (Si) and carbon (C) with corresponding probability of occurrence assuming the Si (or C) sites are all equivalent. There are 455 possible combinations in total. The drawings are purely for visualization and do not show an exact perspective of the crystal.

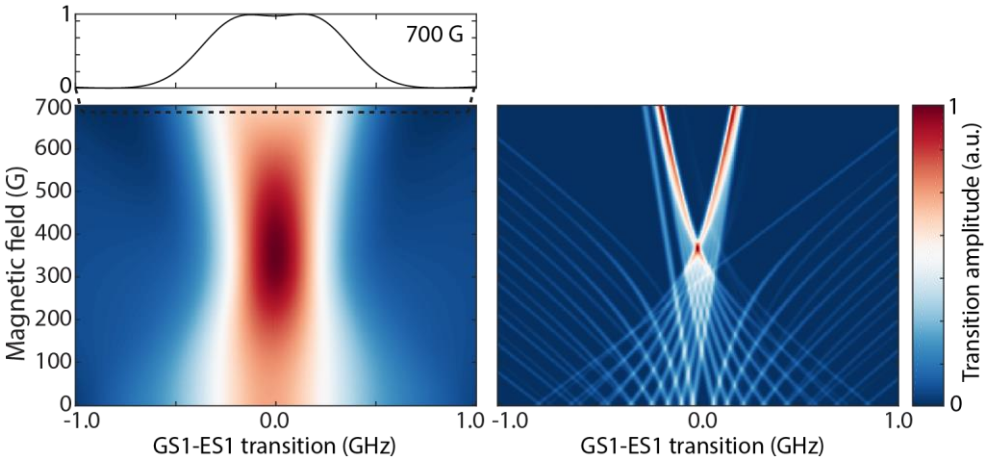

Fig. S3. Simulated optical spectrum for the 4H-SiC α site ES1-GS1 transition. Left: Transition amplitude calculated from the sum of all transitions between the 16 electron and nuclear spin states in the orbital ground and excited states. We use the spin Hamiltonians of GS1 and ES1 obtained in Fig. S4 and considering a 400 MHz inhomogeneous linewidth for every single transition. The simulated signal at 700 G is extracted for comparison with the optical spectrum of a single defect in Fig. 2C. Right: Simulation considering a 20 MHz inhomogeneous linewidth showing all the involved hidden transitions.

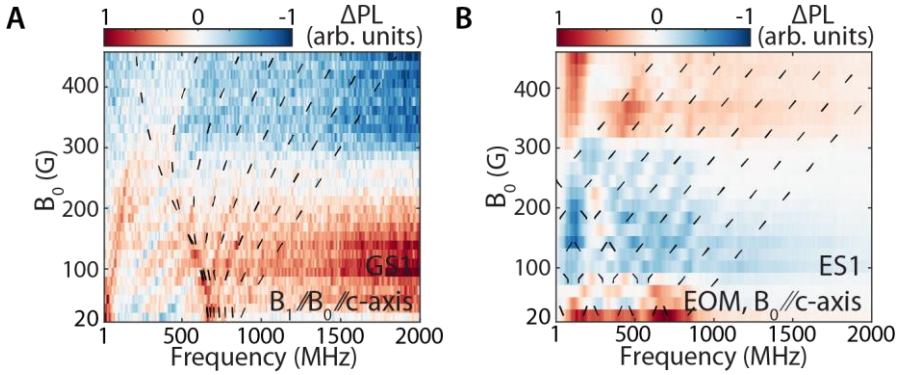

Fig. S4. Spin properties of 4H-SiC α site at 3.4 K. (**A**) ODMR of GS1. (**B**) Pump-probe (hole recovery) experiment. The dashed lines in black are simulated from the fitted spin model. The ODMR signal in (A) also shows contribution from ES1 (blue lines at low frequencies and magnetic fields) which helps fit the spin parameters.

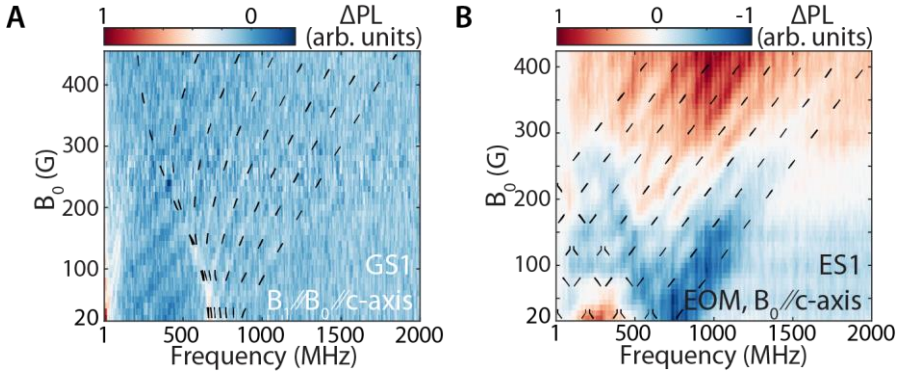

Fig. S5. Spin properties of 6H-SiC α site at 3.4 K. (**A**) ODMR of GS1. (**B**) Pump-probe (hole recovery) experiment. The dashed lines in black are simulated from the fitted spin model. The ODMR signal in (A) also shows contribution from ES1 (blue lines at low frequencies and magnetic fields) which helps fit the spin parameters.

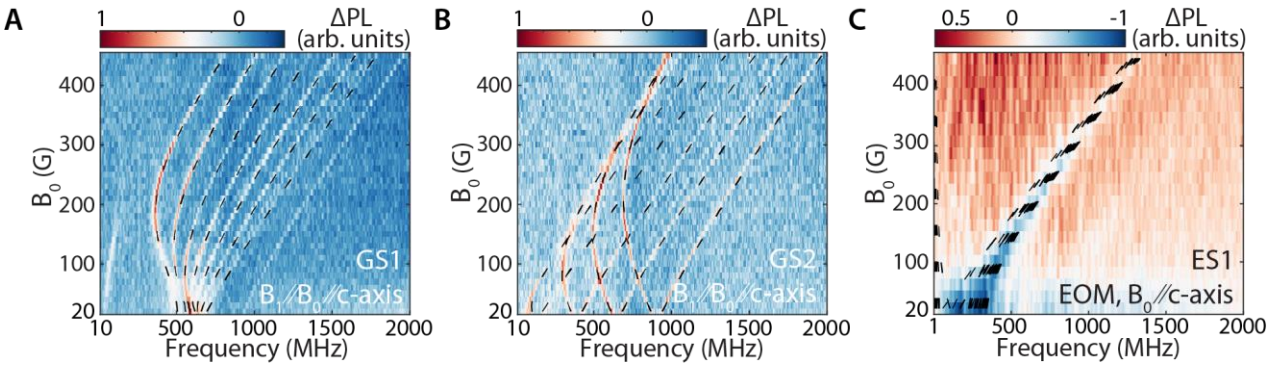

Fig. S6. Spin properties of 6H-SiC β site at 3.4 K. (**A**) ODMR of GS1. (**B**) ODMR of GS2. (**C**) Pump-probe (hole recovery) experiment. The dashed lines in black are simulated from the fitted spin model.

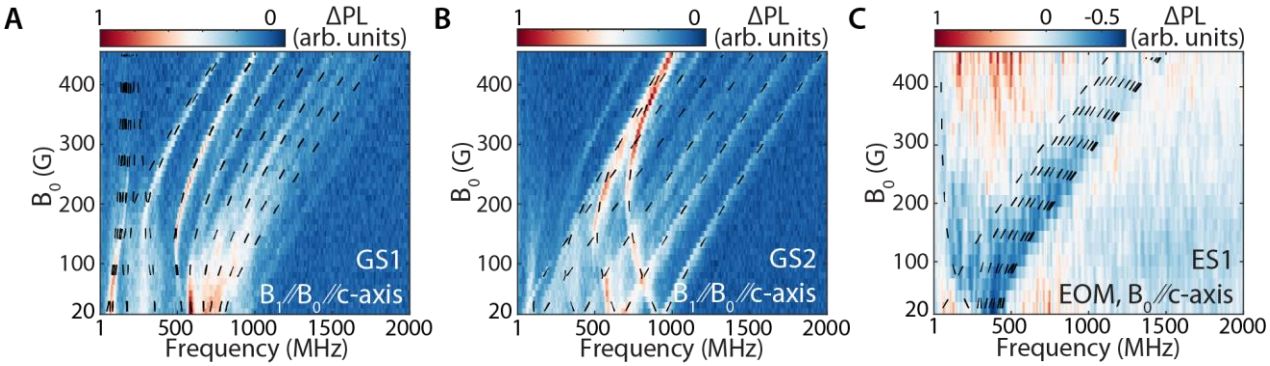

Fig. S7. Spin properties of 6H-SiC γ site at 3.4 K. (**A**) ODMR of GS1. (**B**) ODMR of GS2. (**C**) Pump-probe (hole recovery) experiment. The dashed lines in black are simulated from the fitted spin model.

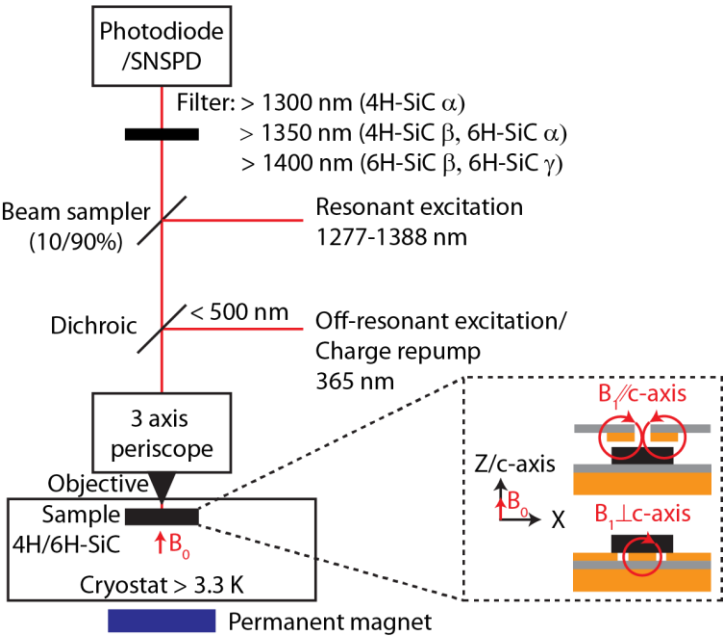

Fig. S8. Schematic of the confocal microscopy setup. The optical paths for excitation and collection are shown in red. The excitation is filtered from the detection by a combination of the beam sampler and filters. Mapping for single defects is realized by moving the 3-axis periscope. A permanent magnet outside the cryostat provides the static magnetic field B_0 and is placed on a calibrated linear translation stage to sweep the field intensity. The sample is placed on a printed circuit board (grey area in dashed box) on a copper cold finger. The board has a microwave stripline (bottom) for microwave driving (B_1) orthogonal to the c-axis, and a secondary board (top) with a coplanar loop antenna for microwave driving parallel to the c-axis.

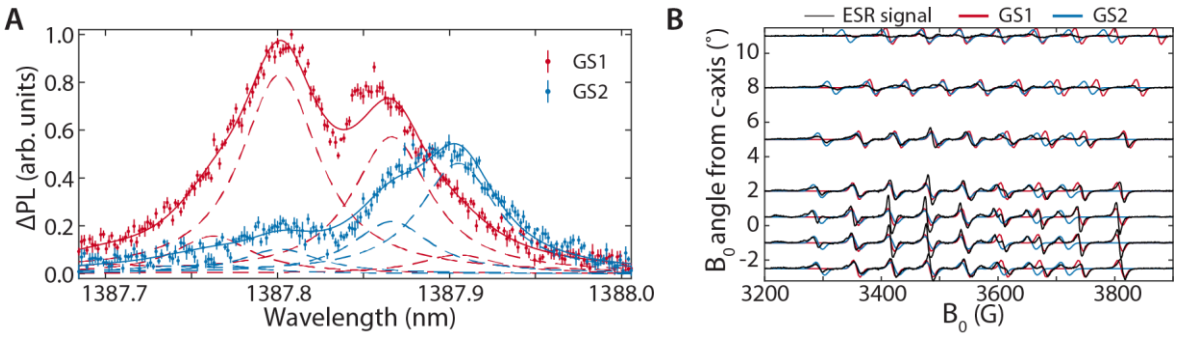

Fig. S9. Additional spectroscopy for the 6H-SiC γ site at 3.4 K. (**A**) ODMR-resolved resonant optical spectroscopy. In red, the microwave drive frequency and static magnetic field are tuned to a spin transition in the GS1 state, while in blue they are tuned to a spin transition in the GS2 state. Four separate transitions can be resolved and fitted compared to only two transitions in direct PL measurements (Fig. 1(C) in the main text). The lineshape for each transition uses the isotope model. (**B**) ESR spectroscopy showing two sets of peaks that are matched by the GS1 (red) and GS2 (blue) spin parameters of the 6H-SiC γ site extracted from the ODMR experiments in Fig. S7.

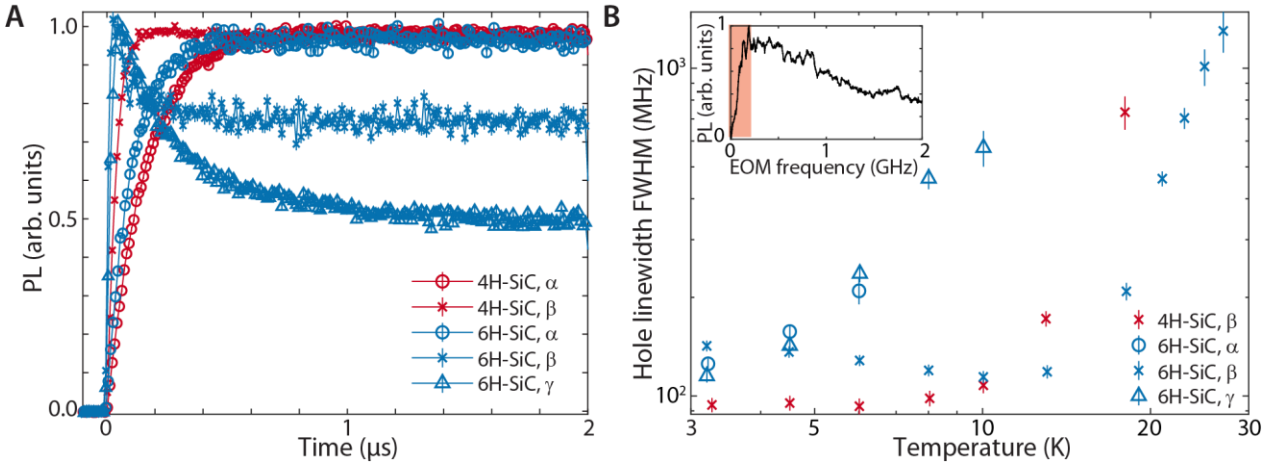

Fig. S10. Optical hole burning experiments. (**A**) Transient detection at 3.3 K of the PL during laser excitation on resonance with the GS1-ES1 transition at time > 0. The PL signal initially rises then decays as the hole is formed. The depth of the decay is related to the lifetime of the shelving state involved in the process. For the α sites, minimal hole burning (depth) is observed, in agreement with the small ODMR contrast in Fig. S4 and S5. (**B**) Full width at half maximum (FWHM) hole linewidth measurement as a function of temperature. This linewidth is obtained by fitting the hole created during pump-probe (EOM) scans as shown in the inset.